



OPEN

DATA DESCRIPTOR

# Intracranial aneurysm CTA images and 3D models dataset with clinical morphological and hemodynamic data

Miao Song<sup>1,7</sup>, Simin Wang<sup>1,7</sup>, Qian Qian<sup>2</sup>, Yuan Zhou<sup>3</sup>, Yi Luo<sup>4</sup> & Xijun Gong<sup>5,6</sup>✉

Intracranial aneurysm is a cerebrovascular disease associated with a high rupture risk, often resulting in death or severe disability. Recent advances in AI enable the prediction of intracranial aneurysm initiation, progression, and rupture through medical image analysis. Despite growing research interest, there is a shortage of publicly available datasets for training and validating AI models. This paper presents a comprehensive dataset comprising high-resolution CTA images of 99 patients with 105 MCA aneurysms and 44 normal healthy controls, along with their respective clinical data and 3D models of aneurysms and the parent arteries derived from the CTA images. Furthermore, recognizing the significance of blood hemodynamics on aneurysm development, this dataset also included the morphological and hemodynamic parameters obtained by computational fluid dynamics (CFD) for each patient and healthy control, which can be utilized by researchers without prior CFD experience. This dataset will facilitate hypothesis-driven or data-driven research on intracranial aneurysms, and has the potential to deepen our understanding of this disease.

## Background & Summary

Intracranial aneurysm (IA) is a common life-threatening disease, with a rupture leading to aneurysmal subarachnoid hemorrhage (SAH) and a mortality rate exceeding 40%<sup>1</sup>. Investigating the development and rupture of aneurysms has been a longstanding research focus. It is reported to be associated with hemodynamics, vascular morphology, and many clinical factors, such as gender, aging, hypertension, smoking, alcohol use, cerebrovascular disease history, and family SAH history<sup>2–4</sup>.

Machine learning is increasingly employed in aneurysm research<sup>5–8</sup>, focusing on factors such as hemodynamics, morphology, and clinical parameters<sup>9–15</sup>. However, access to comprehensive datasets is crucial for model training and systematic comparisons. While notable datasets like ISUIA<sup>16</sup>, ISAT<sup>17</sup>, and UCAS<sup>18</sup> offer epidemiological and genetic insights, they often lack sufficient imaging data for machine learning analysis.

Through extensive literature searches from 2010 to 2024, twelve open databases were identified based on two criteria: 1) open accessibility and 2) inclusion of imaging data or imaging-derived data. The Notable databases include Aneurisk (2012)<sup>19</sup>, AneuX (2022)<sup>20</sup>, Dataset: IntrA (2020)<sup>21</sup>, Pozo *et al.*<sup>22</sup>, Vivanco-Suarez *et al.*<sup>23</sup>, Open data: TOF-MRA (2023)<sup>24</sup>, and several image dataset provided by challenges such as CFD Rupture series (2012–2015)<sup>25–27</sup>, MATCH 2018 I<sup>28</sup> and II<sup>29</sup>, ADAM 2020<sup>30</sup>, and CADA 2020<sup>31</sup> (For a detailed discussion, See Table 1). Crucial initiatives include global efforts to define Common Data Elements for Subarachnoid Hemorrhage and Unruptured Intracranial Aneurysms<sup>32–36</sup>, alongside endeavors by the International Stroke Genetics Consortium and the Aneurysm Data Bank. These initiatives aim to ensure that data are findable, accessible, interoperable, and reusable for advancing aneurysm research.

<sup>1</sup>College of Information Engineering, Shanghai Maritime University, Shanghai, 201306, China. <sup>2</sup>Yunnan Key Laboratory of Computer Technology Applications, Faculty of Information Engineering and Automation, Kunming University of Science and Technology, Kunming, 650504, China. <sup>3</sup>Logistics Engineering College, Shanghai Maritime University, Shanghai, 201306, China. <sup>4</sup>Department of Radiology, the First Affiliated Hospital of University of Science and Technology of China, Hefei, Anhui, 230036, China. <sup>5</sup>Department of Radiology, the Second Affiliated Hospital of Anhui Medical University, Hefei, Anhui, 230032, China. <sup>6</sup>Medical Imaging Center, Anhui Medical University, Hefei, Anhui, 230032, China. <sup>7</sup>These authors contributed equally: Miao Song, Simin Wang. ✉e-mail: [gxj0306@126.com](mailto:gxj0306@126.com)

Category	Project	Image(Type)*	3D Models	Clinical Parameters (Cases)	Morphological Parameters (Cases)	Hemodynamic Parameters (Cases)
Open Data	Aneurisk (2012) <sup>19</sup>	23(3DRA)	103	7(99)	32(103)	22(8)
	Pozo <i>et al.</i> <sup>22</sup>	50(3DRA)	50	3(50)	NA	NA
	Intra (2020) <sup>21</sup>	NA	103	NA	NA	NA
	Vivanco-Suarez <i>et al.</i> <sup>23</sup>	NA**	NA	41(126)	5(141)	NA
	AneuX (2022) <sup>20</sup>	NA	750	6(750)	170(750)	NA
	Di Noto <i>et al.</i> <sup>24</sup>	284(TOF-MRA)	NA	NA	NA	NA
Challenge	CFD Rupture 2012 <sup>25</sup>	NA	1	NA	2(1)	NA
	CFD Rupture 2013 <sup>26</sup>	NA	2	4(2)	4(2)	NA
	CFD Rupture 2015 <sup>27</sup>	5(Micro-CT)	NA	NA	NA	NA
	MATCH 2018 I and II <sup>28,29</sup>	1(3DRA)	NA	NA	NA	NA
	ADAM 2020 <sup>30</sup>	254(TOF-MRA)	NA	NA	NA	NA
	CADA 2020 <sup>31</sup>	131(3DRA)	NA	NA	NA	NA

**Table 1.** Detailed Comparison of Data Types and Parameters in Existing Aneurysm Databases. \* 3DRA refers to three-dimensional digital subtraction angiography. TOF-MRA stands for Time-Of-Flight Magnetic Resonance Angiography. Micro-CT refers to micro-Computed Tomography. \*\* The images provided in this article are Digital Subtraction Angiography(DSA) images in JPEG format, embedded within a PowerPoint(PPTX) file.

Despite their remarkable contributions, these datasets possess certain limitations. Few datasets provide both clinical and raw imaging data, accompanied by comprehensive analyses of aneurysm morphology and hemodynamics for each case. For example, while the Intra dataset offers 3D models of aneurysms and segments, it lacks clinical and imaging data. Similarly, the TOF-MRA dataset exclusively offers raw MRA images. The absence of morphological and hemodynamic analyses also impedes researchers’ understanding of these critical aspects, especially for those lacking specialized expertise in 3D modeling or computational fluid dynamics.

To address these issues, we have constructed an open-access 3D middle cerebral artery (MCA) aneurysm dataset. MCA is a prevalent location for intracranial aneurysms, accounting for 36% of cases<sup>18</sup>. This dataset includes the patient’s clinical data, raw CTA images, and their corresponding derived 3D models (aneurysm-artery and aneurysm models). Additionally, considering the complexity and time required for morphological and hemodynamic analysis, we further measured these parameters for all 3D models to facilitate future research. Finally, in order to enable the comparative research between aneurysm patients and healthy individuals, we have included the healthy MCA vessel in the dataset, processed in the same manner as the aneurysm patients. In summary, our primary contributions are:

1. We propose an open and comprehensive database of MCA aneurysms, allowing researchers to select specific data as needed. Additionally, all 3D models were processed as meshes, enabling researchers to perform their own morphological and hemodynamic analyses. What’s more, our dataset comprises both patients and healthy controls, facilitating comparative analyses.
2. We have conducted an in-depth analysis of the Aneurysms in the dataset, documenting Clinical information, Morphological characteristics, and Hemodynamic data for the patients (termed as CMHA). This comprehensive information serves as a valuable resource for future investigations by researchers.

Methods

**Subjects.** The data for this study were collected retrospectively as part of standard clinical care, with ethical approval granted by the Ethics Committee of the Second Affiliated Hospital of Anhui Medical University (approval number YX2022-021). Due to the retrospective nature of the study and the full anonymization of the dataset, the committee granted a waiver of informed consent for data analysis and public sharing. To comply with data protection regulations, all personal identifiers (e.g., names, dates of birth, addresses, and medical record numbers) were removed. Additionally, imaging data in DICOM format were converted to NIfTI (.nii) format, with all metadata and identifiable features obscured to ensure complete anonymity. To further protect privacy, we applied a threshold filtering algorithm with a threshold of 50 Hounsfield Units (HU), removing soft tissue and facial fat while preserving vascular structures and cranial bones, ensuring no identifiable facial features remain.

A total of 1021 consecutive patients, who underwent head computed tomography angiography (CTA) examinations between January 2012 and January 2018 from the Second Affiliated Hospital of Anhui Medical University in China, were used as a potential data pool. Following the below inclusion criteria: (1) confirmed diagnosis of saccular MCA aneurysms; (2) high-quality images without artifacts, accurately representing the aneurysm and parent artery, with available medical records; (3) absence of dissecting aneurysms and other vascular diseases, such as arteriovenous malformation, moyamoya disease, and arteriovenous fistula. The 143 subjects (99 patients and 44 healthy controls) with 105 IAs (77 ruptured and 28 unruptured) were included in the database (see Table 2 for their demographic information).

	Patients	Healthy controls	Whole sample
Number	99 (70F)	44 (12F)	143 (82F)
Age	59.79 ± 10.22	57.95 ± 12.18	59.25 ± 10.82
IA	105	NA	105

**Table 2.** Demographic Information of the Database.

**Procedure.** Figure 1 illustrates the schematic procedure for data acquisition, preprocessing, and postprocessing. The pipeline comprises three steps: (1) Collection of clinical data and CTA images for selected subjects; (2) Extraction of morphological parameters by reconstructing and segmenting 3D surface models of aneurysms and arteries; (3) Acquisition of hemodynamic parameters through Computational Fluid Dynamics (CFD) methods (i.e., constructing 3D volume models, grid division, setting boundary conditions, and extracting hemodynamic parameters). Two research assistants were trained to perform these three steps under the supervision of an experienced radiologist and a CFD expert. Upon completion of these steps, we obtained 3D models and essential morphological and hemodynamic results for both patients and healthy controls, encompassing 17 morphological parameters and 18 hemodynamic parameters crucial for aneurysm development and rupture. Detailed descriptions of each step are presented in the following sections.

**Collection of clinical data and CTA images.** **Clinical data collection:** Medical records were reviewed by an experienced radiologist to gather demographic and clinical information. These parameters include (see Table 3):

- 6 physiological indicators: gender (SNOMED CT: 263495000), age (SNOMED CT: 424144002), systolic blood pressure (SNOMED CT: 399304008), diastolic blood pressure (SNOMED CT: 446226005), heart rate (SNOMED CT: 399017001), and respiratory rate (SNOMED CT: 271625008).
- 6 risk factors for vascular disease: smoker (SNOMED CT: 65568007), drinker of alcohol (SNOMED CT: 219006), hypertension history (SNOMED CT: 161501007), diabetes mellitus (SNOMED CT: 73211009), family history of IA (SNOMED CT: 10624451000119103), and earlier SAH from another aneurysm.
- 2 aneurysm profile: shape and location (include M1 (SNOMED CT: 730651002), M2 (SNOMED CT: 730652009), M3 (SNOMED CT: 772219006), M4 (SNOMED CT: 772221001) and their junctions).
- 2 rupture or growth risk scores: PHASES (Population, Hypertension, Age, Size of aneurysm, Earlier SAH from another aneurysm, Site of aneurysm) and ELAPSS (Earlier subarachnoid hemorrhage, aneurysm Location, Age, Population, aneurysm Size and Shape).

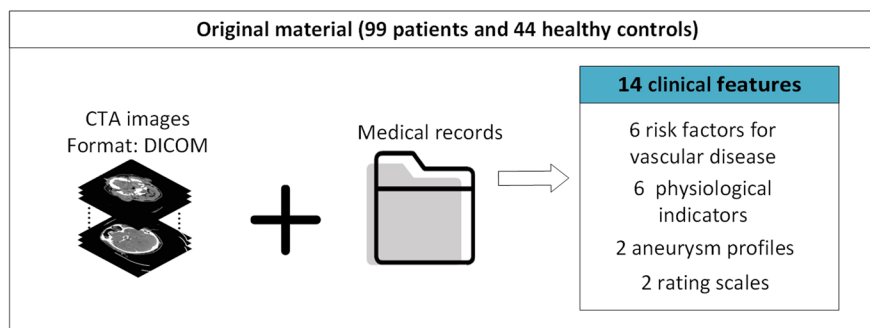
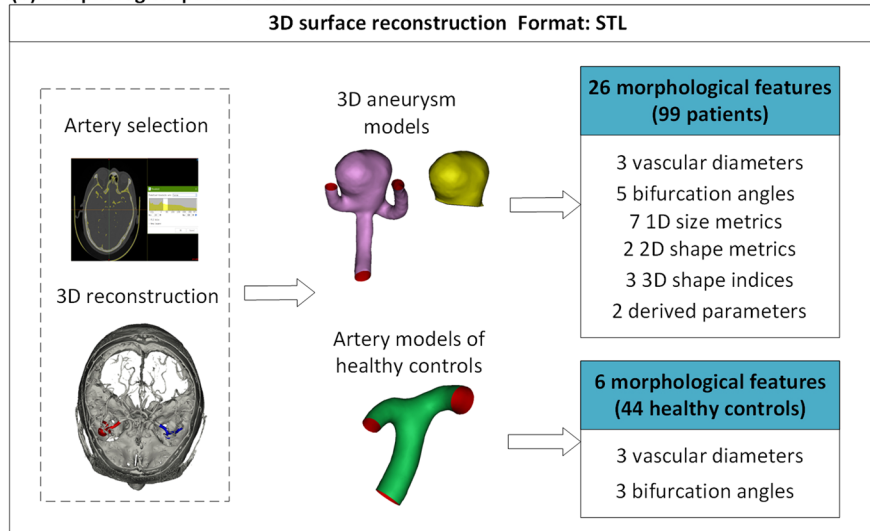
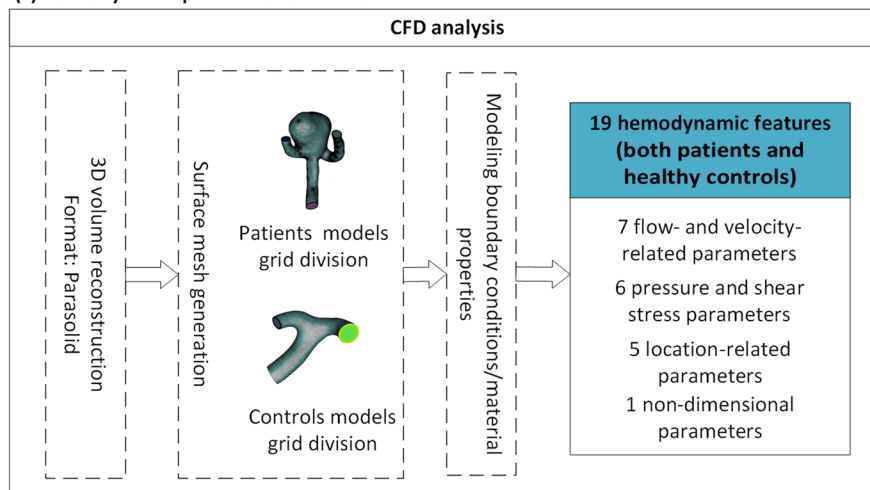
**CTA image collection:** The database comprises 143 head CT scans, each consisting of a conventional CT examination and a CT angiography (CTA). These scans were conducted using either a Philips Intellispace portal 128-row CT or a Siemens force dual-source CT, with a slice thickness of 1.25 mm, an interlayer spacing of 0.625 mm, a tube voltage of 120 kV, a tube current of 240 mA, a field of view measuring 23 cm × 23 cm, and a matrix size of 512 × 512.

**Morphological parameter extraction.** To obtain precise measurements of aneurysm morphology, we used a semi-automated segmentation approach to process CTA images. Arteries and aneurysms were automatically segmented from surrounding brain tissue and bone using predefined threshold values. This was followed by the reconstruction of 3D surface models, which were manually refined by two radiologists. Final morphological measurements were then conducted on these 3D artery and aneurysm models.

**Artery Segmentation Process:** CTA slices from each subject were imported into Mimics 17.0 (Materialise, Belgium) in DICOM format for vessel segmentations. Establishing an appropriate threshold range was crucial at this stage. An inappropriate threshold range could lead to deviations from the vessels' anatomical morphology, particularly affecting smaller or tortuous vessels<sup>37</sup>. Through preliminary experiments and visual observations, an optimal Hounsfield Unit (HU) range of 150–600 was determined. This range was found to yield a precise selection of cerebral arterial vessels and MCA aneurysms (see Fig. 2(a)). For specific challenges, such as vessel adherence to aneurysms (approximately 10% of cases), research assistants manually refined the region of interest (ROI) using segmentation tools in collaboration with expert radiologists, ensuring higher precision and consistency.

**Reconstruction of 3D surface models:** The threshold established in the previous step automatically generated an initial 3D surface model using the region-growing segmentation algorithm. However, automatic segmentation might introduce topological defects and inaccuracies, especially in images with non-uniform intensity.

To enhance model accuracy, we executed a three-step refinement process. First, within Mimics, the erasing tool, including lasso and rectangle functions, was used to eliminate branches in the MCA region that did not directly affect blood flow and to separate vascular blending artifacts<sup>38</sup>. Next, 3-matic Research 13.0 software (Materialise, Belgium) was employed to remove protrusions and smooth the surface mesh. According to our protocol, the length of the inlet segment had to exceed that of the two outlet segments, with minimum lengths of 6 mm for the inlet and 3 mm for the outlets. Finally, three vascular ports were trimmed to create a closed surface mesh, essential for defining inflow and outflow parameters for subsequent computational fluid dynamics (CFD) simulations. The final 3D models—including the aneurysm-artery model, aneurysm model, and healthy control model—were exported in STL format (see Fig. 2(b)).

**(a) Clinical data and CTA images collection****(b) Morphological parameters extraction****(c) Hemodynamic parameter extraction**

**Fig. 1** Pipeline of data processing. **(a)** Collection of clinical data and CTA images. **(b)** Morphological parameter extraction, involving three procedures: Artery Selection, 3D surface reconstruction, and measurements of morphological parameters. **(c)** Hemodynamic parameter extraction, involving four procedures: 3D volume reconstruction, surface mesh generation, modeling boundary conditions and material properties, and computation of hemodynamic parameters.

The segmented aneurysms were independently reviewed by two radiologists, focusing on anatomical accuracy and ensuring no defects were introduced during segmentation. Any discrepancies, such as variations in aneurysm borders or segmentation errors, were resolved through re-segmentation if necessary, ensuring the final models accurately represented the aneurysm and surrounding vessels.

Category	Feature name	Description	Patients n=99	Controls n=44
6 physiological indicators	Gender	M - male; F - female	70F	12F
	Age	Positive integer $\in [27,83]$	$59.8 \pm 10.359$	$57.95 \pm 12.179$
	Systolic pressure	Measured at admission	$152.49 \pm 26.522$	$140.7 \pm 27.276$
	Diastolic pressure	Measured at admission	$88.94 \pm 13.519$	$83.52 \pm 17.611$
	Heart rate	Resting heart rate	$80.81 \pm 13.721$	$73.77 \pm 9.562$
	Respiratory rate	Admission Respiratory Rate	$19.75 \pm 2.238$	$18.48 \pm 1.023$
6 risk factors for vascular	Smoker	1 - Yes; 0 - No	5	9
	Drinker of alcohol	1 - Yes; 0 - No	7	12
	Diabetes mellitus	1 - Yes; 0 - No	9	8
	Hypertension history	1 - Yes; 0 - No	67	27
	Family history of IA	1 - Yes; 0 - No	2	1
	Earlier SAH from another aneurysm	1 - Yes; 0 - No	0	0
2 aneurysm profiles	Shape	1 - irregular; 0 - regular	68	0
	Location	MCA specific different segments	M1,M2,M3, and junction	NA
2 rating scales	PHASE	To predict a patient's risk of aneurysm rupture	$2.08 \pm 0.829$	NA
	ELAPSS	To assess the risk of aneurysm growth in patients with UIA	$4.80 \pm 0.447$	NA

**Table 3.** Clinical Data Summary for 99 Patients and 44 Healthy Controls.

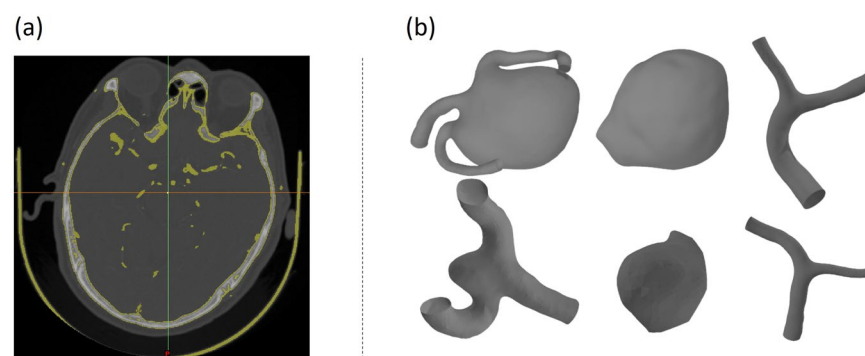


**Fig. 2** (a) Artery selection. Cerebral arterial vessels (highlighted in yellow) are distinctly delineated from the surrounding brain tissue (in grey) and bone structures (in white). (b) Generated 3D surface models. The models are respectively labeled as follows from left to right: aneurysm-artery models (comprising both aneurysm and artery), aneurysm models, and healthy control models, and they were exported in STL format.

**Morphological parameters collection:** We selected a subset of 26 parameters (see Table 4) based on the morphological parameters reported by Hellmeier<sup>39</sup> and Dhar<sup>40</sup>. Of these, six parameters, including the three vascular diameters, aneurysm neck circumference, maximum aneurysm length ( $L_1$ ), and maximum aneurysm width ( $L_2$ ), were manually measured using the 'spline' and 'measure' tools within Mimics, based on the 3D surface model. The remaining 20 parameters were automatically computed using the vmtk4aneurysms toolbox (<https://github.com/iagolessa/vmtk4aneurysms>) and the Vascular Modeling Toolkit (VMTK) (<http://www.vmtk.org/>). Figure 3(a) depicts the schematic for measuring some of these parameters. These parameters include:

- 3 vascular diameters: the parent artery diameter ( $D$ ), the thicker branch diameter ( $D_1$ ), and the smaller branch diameter ( $D_2$ ).
- 5 bifurcation angles: angles between the aneurysm and the two branches ( $\theta_1, \theta_2$ ), the vessel angle between the two branches ( $\gamma$ ), and angles between the parent artery and the two branches ( $\gamma_1, \gamma_2$ ) (For details of vascular angle measurements, see the supplementary file).
- 7 1D size metrics: aneurysm perpendicular height ( $H$ ), neck width ( $NW$ ), maximum length of the aneurysm ( $L_1$ ), maximum width of the aneurysm ( $L_2$ ), neck circumference ( $NC$ ), neck surface area ( $NS$ ), and Maximum Diameter ( $D_{max}$ ).
- 2 2D shape metrics: bottleneck factor and conicity parameter.
- 4 3D size metrics: aneurysm volume ( $V$ ), aneurysm surface area, hull surface area, and hull volume.
- 3 3D shape indices: ellipticity index, non-sphericity index, and undulation index.
- 2 derived parameters: aspect ratio ( $AR$ ), calculated as  $H/NW$ , following Ujiie<sup>41</sup> and Dhar<sup>40</sup>, and size ratio ( $SR$ ), defined as  $H / ((D + D_1 + D_2) / 3)$ , following Kashiwazaki<sup>42</sup>.



Category (unit)	Feature name	Description	Patients n=99	Controls n = 44
3 vascular diameters	$D$	Diameter of the parent artery	$3.09 \pm 0.57$	$2.66 \pm 0.47$
	$D_1$	Diameter of the thicker branch artery	$2.12 \pm 0.56$	$1.85 \pm 0.46$
	$D_2$	Diameter of the smaller branch arteries	$2.59 \pm 0.56$	$1.99 \pm 0.50$
5 bifurcation angles	$\theta_1$	Angle between the aneurysm and the thicker branch (branch 1)	$106.25 \pm 27.31$	NA
	$\theta_2$	Angle between the aneurysm and the smaller branch (branch 2)	$108.39 \pm 24.48$	NA
	$\gamma$	Angle between branch 1 and branch 2	$128.01 \pm 28.99$	$91.99 \pm 14.37$
	$\gamma_1$	Angle between the parent artery and branch 1	$124.07 \pm 23.27$	$136.99 \pm 13.46$
	$\gamma_2$	Angle between the parent artery and branch 2	$105.94 \pm 24.53$	$131.00 \pm 10.10$
7 1D Size Metrics	NW	Maximum distance between two points on the neck perimeter	$4.91 \pm 1.46$	NA
	H	Maximum perpendicular distance from the neck plane to the aneurysm surface	$4.38 \pm 2.94$	NA
	$L_1$	Maximum aneurysm length parallel to the aneurysm neck	$5.17 \pm 3.09$	NA
	$L_2$	Maximum aneurysm width perpendicular to $L_1$	$5.55 \pm 2.87$	NA
	NC	Circumference of the aneurysm neck	$17.82 \pm 5.64$	NA
	NS	Area of the aneurysm neck	$23.08 \pm 14.55$	NA
	$D_{max}$	Maximum neck plane-parallel distance between two points on the aneurysm surface	$5.86 \pm 2.50$	NA
2 2D Shape Metrics	Bottleneck factor	Ratio of maximum diameter to maximum neck diameter	$1.16 \pm 0.22$	NA
	Conicity parameter	Measures where the widest cross-section occurs: $CP = 0.5 H_b/H$ , where $H_b$ is the height of the cross-section from the neck plane at which Maximum Diameter occurs.	$0.35 \pm 0.19$	NA
4 3D Size Metrics	V	Volume of the aneurysm	$157.49 \pm 341.86$	NA
	Aneurysm surface area	Surface area of the aneurysm	$102.79 \pm 135.25$	NA
	Hull surface area	Surface area of the aneurysm's convex hull	$103.26 \pm 137.98$	NA
	Hull volume	Volume of the aneurysm's convex hull	$165.75 \pm 355.24$	NA
3 3D Shape Indices	Ellipticity index	Normalised ratio of convex hull volume to convex hull surface area relative to a hemisphere	$0.1 \pm 0.04$	NA
	Non-sphericity index	Normalised ratio of volume to surface area relative to a hemisphere	$0.11 \pm 0.05$	NA
	Undulation index	1 minus the ratio of volume to convex hull volume	$0.04 \pm 0.03$	NA
2 derived variables	AR	$H/NW$	$0.84 \pm 0.40$	NA
	SR	$H / ((D + D_1 + D_2) / 3)$	$0.95 \pm 0.32$	NA

**Table 4.** Morphological Parameters Summary for 99 Patients and 44 Healthy Controls.

Each manually measured morphological parameter underwent two independent measurements by trained assistants, and the resulting average value was used for subsequent analysis.

**Hemodynamic parameters extraction.** To obtain precise and dependable hemodynamic parameters, we employed a systematic approach encompassing the reconstruction of 3D volume models, surface mesh generation, modeling of boundary conditions and material properties, and the computation of hemodynamic parameters using the Navier-Stokes equations.

**Reconstruction of 3D volume models:** The initial 3D surface models, acquired previously, were further refined using Geomagic Studio 2015 software (Geomagic Corporation, USA). Following noise reduction, mesh refinement, cutting, and smoothing, these refined models were then imported into UG NX 11.0 software (Siemens PLM Software, Germany) in Parasolid format. This step facilitated the encapsulation of the vessel model's watershed, resulting in the creation of a final 3D volume model in Parasolid format.

**Surface mesh generation and boundary conditions:** Fluid and solid grids were separately constructed based on the 3D volume model using Fluent 2020 R2 (ANSYS Inc., USA). The grid size ranged between 0.1 mm and 0.3 mm, resulting in the creation of 300000 to 1 million finite volume element grids for CFD simulations. This ensured a high mesh quality with good triangle edge ratio and homogeneous triangle sizes, promoting stability and convergence in the simulation computations.

The blood was assumed to be a Newtonian fluid with a density of  $1060 \text{ kg/m}^3$ <sup>43–45</sup> and dynamic viscosity of  $0.004 \text{ Pa} \cdot \text{s}$ <sup>46</sup>. The governing equations were the incompressible Navier-Stokes equations<sup>47</sup>. Moreover, considering the thinning of arterial walls caused by the presence of an aneurysm<sup>48</sup>, a uniform wall thickness of 0.3 mm was assumed for all models in the current study, deviating slightly from the normal arterial wall thickness of approximately 0.36 mm.

The inlet and outlet were configured as fixed boundary conditions, while a no-slip boundary condition was applied to the blood vessel wall. The inlet flow velocity, which represents the average blood flow velocity

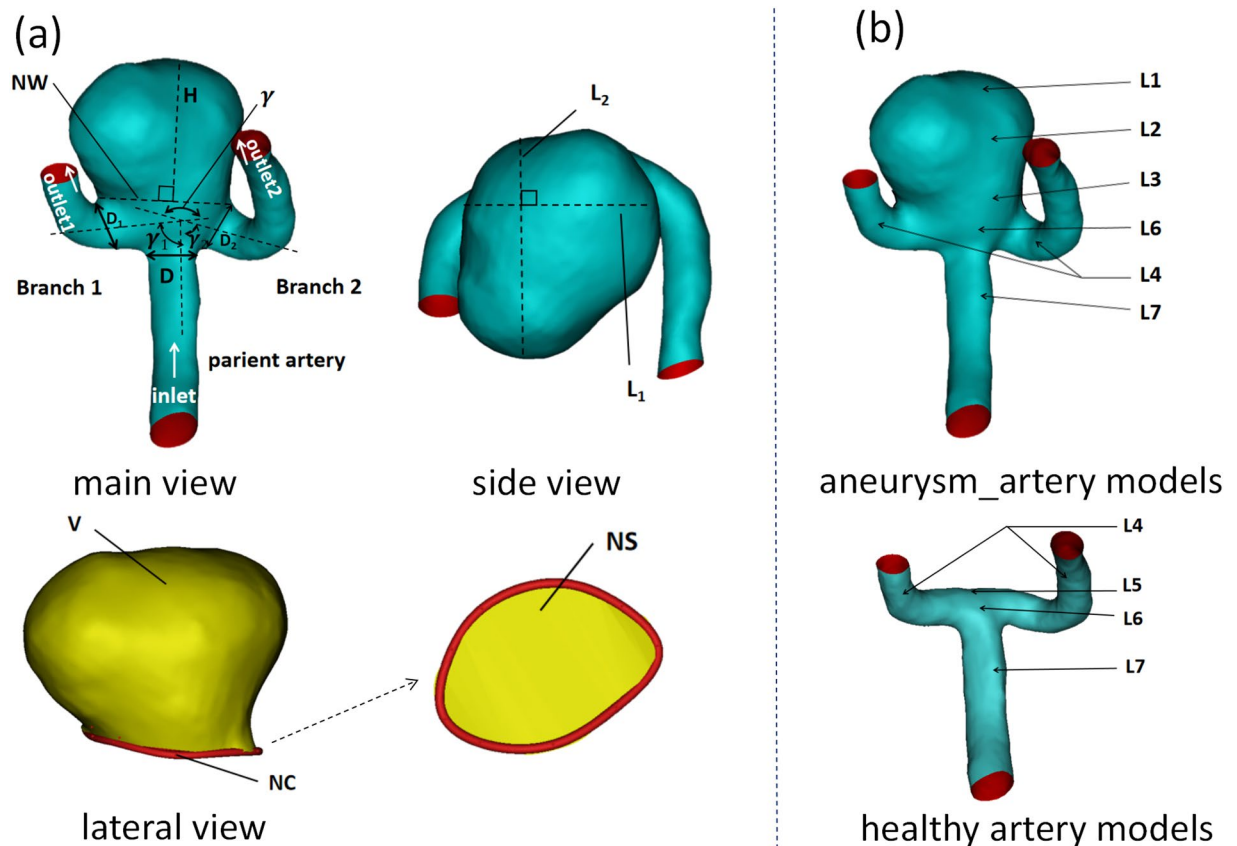


**Fig. 3** (a) Definitions of morphological parameters in the main view, side view, and lateral view. (b) Different locations of aneurysm-artery models and healthy artery models. To precisely indicate the extreme values' locations, aneurysm models were divided into seven regions: aneurysm dome fundus (L1), aneurysm equatorial region (L2), aneurysm neck (L3), branch vessel (L4), aneurysm bifurcation (L5), bifurcation vicinity (L6), and mid-segment of the parent artery (L7).

over a cardiac cycle, is critical for our simulations. This parameter was adjusted according to age and gender, following the methodology outlined by Alwatban's model<sup>49</sup> (Male:  $v_m = 65.41 - 0.26 \times \text{Age}$ ; Female:  $v_m = 65.41 - 0.26 \times \text{Age}$ ). This approach is intended to more accurately reflect the physiological variances observed in real-world scenarios. The outlet back pressure was set at 13,332 Pa (equivalent to 100 mmHg). In terms of the flow regime, Geers<sup>50</sup> and Xiang<sup>11</sup> have demonstrated that steady flow can effectively approximate plausible flow and stress patterns in their average states. Therefore, steady flow is utilized instead of pulsatile flow for this simulation.

**Hemodynamic Parameters Collection:** We computed a total of 19 hemodynamic parameters across four categories from the simulated flow fields (see Table 5).

The first category comprises 7 flow- and velocity-related parameters: inlet mass flow rate ( $\text{kg} \cdot \text{s}^{-1}$ ), two outlet mass flow rates ( $\text{kg} \cdot \text{s}^{-1}$ ), two outlet mass flow ratios, maximum velocity ( $\text{m} \cdot \text{s}^{-1}$ ), and mean velocity ( $\text{m} \cdot \text{s}^{-1}$ ).

The second category encompasses 6 mean pressure and shear stress parameters: Mean wall pressure (Pa), mean internal pressure (Pa), mean wall shear stress (Pa), mean wall pressure gradient ( $\text{kg} \cdot \text{m}^{-2} \cdot \text{s}^{-2}$ ), mean internal pressure gradient ( $\text{kg} \cdot \text{m}^{-2} \cdot \text{s}^{-2}$ ), and mean wall shear stress gradient ( $\text{kg} \cdot \text{m}^{-2} \cdot \text{s}^{-2}$ ).

The third category comprises 5 parameters related to extreme values and their respective locations (See Fig. 3(b) for the location demonstration of aneurysm). They are the Max wall pressure (Pa), max WSS (Pa), min WSS (Pa), max wall pressure gradient ( $\text{kg} \cdot \text{m}^{-2} \cdot \text{s}^{-2}$ ), max WSS gradient ( $\text{kg} \cdot \text{m}^{-2} \cdot \text{s}^{-2}$ ), along with their corresponding positions. These parameters are important for capturing extreme flow dynamics and play a critical role in predicting the development and rupture of an aneurysm.

Additionally, we collected 1 non-dimensional parameter: Oscillatory shear index.

It's worth noting that extreme values of pressure and shear stress may occasionally appear at the distal inlet and outlet regions of the model, rather than in proximity to the aneurysms, as illustrated by the red area at the inlet in Fig. 4(d). This discrepancy can be attributed to interactions between incomplete mesh distribution and boundary conditions near the inlet or outlet during the CFD simulation process<sup>51,52</sup>. To ensure the accuracy and reliability of the results, we conducted rigorous visual inspections to pinpoint extreme values and their spatial locations. Subsequently, these values were systematically ranked in ascending order, with those occurring at the outlet and/or inlet or in unreasonable locations being excluded, thus yielding valid results.

Category	Feature name	Description	Patients n = 99	Controls n = 44
7 flow- and velocity-related parameters	Inlet mass flow	The volume of fluid entering the inlet per unit time	0.0045 ± 0.0019	0.0032 ± 0.0011
	Outlet 1 mass flow	The fluid mass passing through the outlet of the thicker branch per unit time	− 0.0027 ± 0.0015	− 0.002 ± 0.00083
	Outlet 2 mass flow	The fluid mass passing through the outlet of the thinner branch per unit time	− 0.0018 ± 0.0012	− 0.0011 ± 0.00052
	Outlet 1 mass flow ratio	The ratio of the mass flow in the thicker branch to the inlet mass flow	− 0.58 ± 0.20	− 0.63 ± 0.11
	Outlet 2 mass flow ratio	The ratio of the mass flow in the thinner branch to the inlet mass flow	0.4 ± 0.20	− 0.36 ± 0.11
	Max velocity	The highest blood velocity	1.50 ± 0.63	1.05 ± 0.33
	Mean velocity	The average blood velocity	0.50 ± 0.18	0.53 ± 0.10
6 mean pressure and shear stress parameters	Mean wall pressure	The average pressure on the vessel wall within the aneurysm or parent artery	13967.62 ± 1618.75	13635.73 ± 292.73
	Mean internal pressure	The average pressure of blood flow within the aneurysm or parent artery	14168.58 ± 961.98	13686.64 ± 366.37
	Mean WSS	Mean wall shear stress of aneurysm or parent artery	16.44 ± 8.49	14.91 ± 5.57
	Mean wall pressure gradient	The average pressure gradient on the vessel wall within the aneurysm or parent artery	119752.33 ± 94604.08	90903.59 ± 49742.35
	Mean internal pressure gradient	The average pressure gradient of blood flow within the aneurysm or parent artery	128721.03 ± 121100.88	84543.76 ± 42215.46
	Mean WSS gradient	The average shear stress gradient on vessel wall within the aneurysm or parent artery.	16168.73 ± 8908.73	15327.79 ± 6570.84
5 location- related parameters	Max wall pressure	The highest pressure on vessel wall within the aneurysm or parent artery	14722.97 ± 1221.79	17033.73 ± 20125.72
	Max WSS	The maximum shear stress on vessel wall within the aneurysm or parent artery	91.65 ± 64.65	48.35 ± 23.64
	Min WSS	The minimum shear stress on vessel wall within the aneurysm or parent artery	0.12 ± 0.17	0.15 ± 0.21
	Max wall pressure gradient	The maximum pressure gradient on vessel wall within the aneurysm or parent artery	1402423.6 ± 1579699.39	610615.86 ± 351211.62
	Max WSS gradient	The maximum shear stress gradient on vessel wall within the aneurysm or parent artery	246807.15 ± 257601.92	100502.15 ± 45725.19
1 non-dimensional parameter	Oscillatory shear index	Measures the directional change of WSS during the cardiac cycle	5.45 ± 2.11	3.18 ± 0.65

**Table 5.** Hemodynamic Parameters Summary for 99 Patients and 44 Healthy Controls.

## Data Records

The dataset is available in the Figshare repository<sup>53</sup>. It includes comprehensive medical imaging data from 99 patients and 44 healthy controls, organized in a standardized manner as depicted in Fig. 5. Each patient's record comprises raw CTA images, 3D models, and hemodynamic analysis results for both the aneurysm and aneurysm-artery models. The data for healthy controls includes raw CTA images and models of healthy arteries. Patient identifiers are uniformly coded with 'AHMU1218', representing Anhui Medical University and the data collection period from 2012 to 2018, followed by a three-digit patient number. The analysis results are organized into five distinct CSV files within the CMHA directory, covering clinical data, morphological parameters for both patients and healthy controls, and hemodynamic parameters for both groups.

## Technical Validation

We implemented the following measures to ensure image quality and data consistency during data collection and the process of morphological and hemodynamic measurements.

**Data Collection.** An expert radiologist from the Second Affiliated Hospital of Anhui Medical University visually inspected the image data quality, ensuring it met acceptable standards. This inspection excluded images with artifacts like pseudo-enhancements and scattering, and confirmed a full brain view without significant motion artifacts.

**Morphological and Hemodynamic Measurements.** Ensuring measurement consistency is essential, as manual measurements can introduce interrater discrepancies during segmentation and the extraction of both morphological and hemodynamic parameters. We conducted a post-segmentation validation to verify the accuracy of segmentation by comparing the segmented aneurysm volume with that reported in medical records, aiming to maintain differences within 5%. In case of significant disparities, we applied remodeling, smoothing, and re-segmentation to the CTA images. If disparities remained unresolved even after these measures, the CTA images were excluded from the dataset. For the morphological parameters, such as artery diameters and angles between arteries, they were measured following a standardized protocol. We independently measured them twice and calculated the average. During obtaining hemodynamic parameters, we manually identified five extreme values along with their corresponding locations. For precision, we performed two separate measurements. If the extreme values were consistent in location across both measurements, we selected the maximum value. In cases



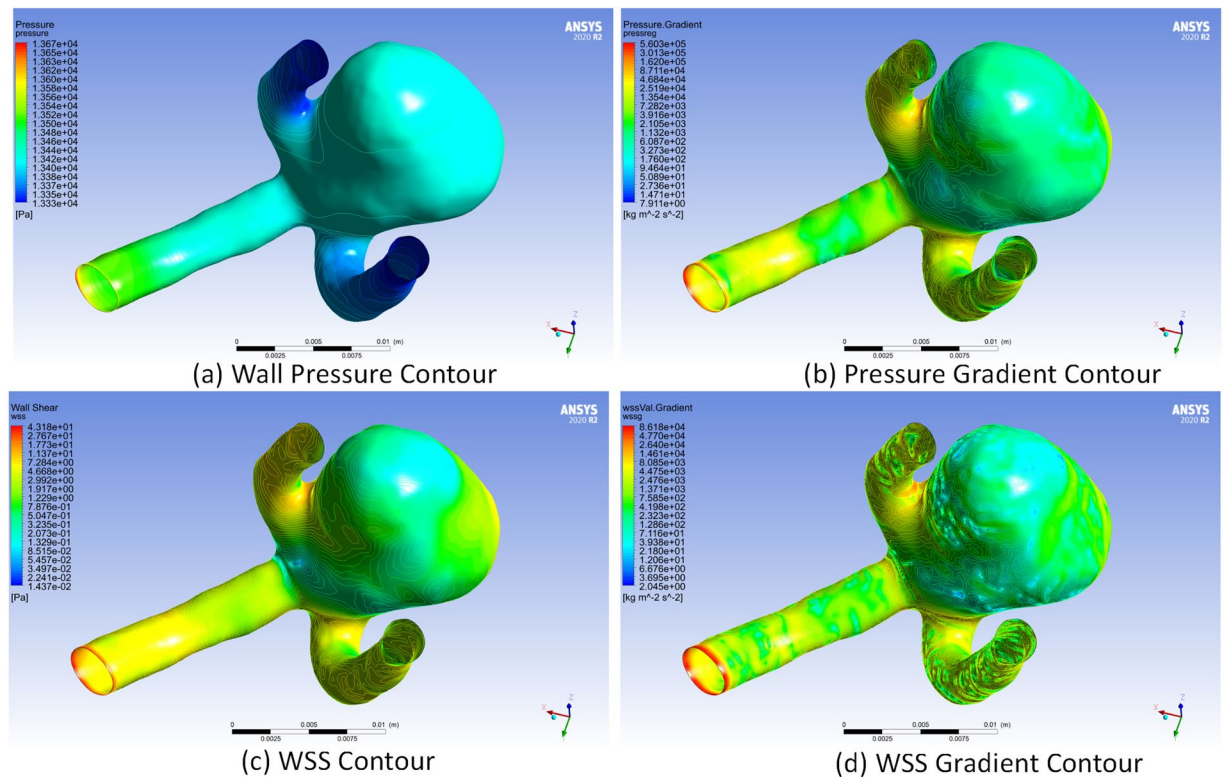


**Fig. 4** The contour graphs of (a) wall pressure, (b) pressure gradient, (c) WSS, and (d) WSS gradient.

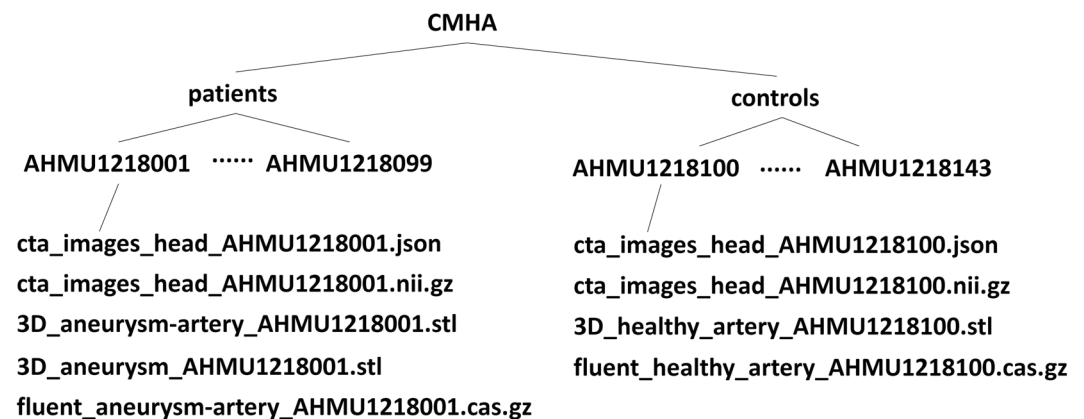


**Fig. 5** File Organization of the Dataset.

where the extreme values differed in location, a different research assistant conducted measurements. We retained the results consistent with this assistant's measurements from the initial two measurements.

### Usage Notes

This database facilitates hypothesis-driven research on intracranial aneurysms. Researchers can compare various parameters and newly developed indicators between patients with aneurysms and healthy controls to investigate the underlying pathological mechanisms. The database also supports data-driven investigations, as it contains comprehensive clinical, morphological, and hemodynamic information, including rupture status labels for each patient. Researchers can select suitable feature sets for training machine learning models to predict aneurysm rupture. Additionally, the dataset includes 3D aneurysm models that enable automatic segmentation and vessel reconstruction.

A limitation of this dataset is the lack of a comprehensive comparison across various teams and software tools. The image segmentation process relies on factors such as the operator's experience, the segmentation procedure, and the software tools used<sup>39</sup>. Our current approach employs a standardized semi-automated method designed to minimize operator-induced variability. However, there may still be some degree of variability in

our results compared to those obtained from different segmentation techniques, particularly in complex cases that require manual intervention. Users need to be aware of these potential implications. For users who employ different segmentation techniques and need to integrate data from diverse sources, it's recommended to evaluate how these variations might impact their results. We advise using unified software, with original NIfTI files as the starting point, to ensure consistency across experiments and enable reliable comparisons. These original NIfTI image files are available for validation and comparative studies with different segmentation methods or software tools.

This dataset is freely accessible under the Open Data Commons Attribution License (CC-BY 4.0): <https://creativecommons.org/licenses/by/4.0/>. Users have permission to copy, share, redistribute, adapt, remix, transform, or build upon the data in any format or medium.

## Code availability

No custom code was utilized in this study. Software tools used for data processing are mentioned in the Methods and Technical Validation sections.

Received: 5 October 2023; Accepted: 31 October 2024;

Published online: 12 November 2024

## References

- De Rooij, N. K., Linn, F. H. H., Van Der Plas, J. A., Algra, A. & Rinkel, G. J. E. Incidence of subarachnoid haemorrhage: a systematic review with emphasis on region, age, gender and time trends. *Journal of Neurology, Neurosurgery & Psychiatry* **78**, 1365–1372 (2007).
- Chung, B. *et al.* Identification of hostile hemodynamics and geometries of cerebral aneurysms: a case-control study. *American Journal of Neuroradiology* **39**, 1860–1866 (2018).
- Hu, S. & Li, M. In reply: a meta-analysis of risk factors for the formation of de novo intracranial aneurysms. *Neurosurgery* **86**, E476 (2020).
- Vlak, M. H., Algra, A., Brandenburg, R. & Rinkel, G. J. Prevalence of unruptured intracranial aneurysms, with emphasis on sex, age, comorbidity, country, and time period: a systematic review and meta-analysis. *The Lancet Neurology* **10**, 626–636 (2011).
- Shi, Z. *et al.* A clinically applicable deep-learning model for detecting intracranial aneurysm in computed tomography angiography images. *Nature communications* **11**, 6090 (2020).
- Ly, N. *et al.* A pilot study using a machine-learning approach of morphological and hemodynamic parameters for predicting aneurysms enhancement. *International Journal of Computer Assisted Radiology and Surgery* **15**, 1313–1321 (2020).
- Kim, H. C. *et al.* Machine learning application for rupture risk assessment in small-sized intracranial aneurysm. *Journal of clinical medicine* **8**, 683 (2019).
- Heo, J. *et al.* Prediction of intracranial aneurysm risk using machine learning. *Scientific reports* **10**, 6921 (2020).
- Juvela, S., Poussa, K. & Porras, M. Factors affecting formation and growth of intracranial aneurysms: a long-term follow-up study. *Stroke* **32**, 485–491 (2001).
- Jiang, P. *et al.* Hemodynamic findings associated with intraoperative appearances of intracranial aneurysms **43**, 203–209 (2020).
- Xiang, J. *et al.* Hemodynamic-morphologic discriminants for intracranial aneurysm rupture. *Stroke* **42**, 144–152 (2011).
- Björkman, J. *et al.* Irregular shape identifies ruptured intracranial aneurysm in subarachnoid hemorrhage patients with multiple aneurysms. *Stroke* **48**, 1986–1989 (2017).
- Lindgren, A. E. *et al.* Irregular shape of intracranial aneurysm indicates rupture risk irrespective of size in a population-based cohort. *Stroke* **47**, 1219–1226 (2016).
- Wermer, M. J., Van Der Schaaf, I. C., Algra, A. & Rinkel, G. J. Risk of rupture of unruptured intracranial aneurysms in relation to patient and aneurysm characteristics: an updated meta-analysis. *Stroke* **38**, 1404–1410 (2007).
- Baek, H., Jayaraman, M. V. & Karniadakis, G. E. Wall shear stress and pressure distribution on aneurysms and infundibulae in the posterior communicating artery bifurcation. *Annals of biomedical engineering* **37**, 2469–2487 (2009).
- Wiebers, D. O. Unruptured intracranial aneurysms: natural history, clinical outcome, and risks of surgical and endovascular treatment. *The Lancet* **362**, 103–110, [https://doi.org/10.1016/S0140-6736\(03\)13860-3](https://doi.org/10.1016/S0140-6736(03)13860-3) (2003).
- Molyneux, A. International subarachnoid aneurysm trial (isat) of neurosurgical clipping versus endovascular coiling in 2143 patients with ruptured intracranial aneurysms: a randomised trial. *The Lancet* **360**, 1267–1274, [https://doi.org/10.1016/S0140-736\(02\)11314-6](https://doi.org/10.1016/S0140-736(02)11314-6) (2002).
- The UCAS Japan Investigators. The natural course of unruptured cerebral aneurysms in a Japanese cohort. *New England Journal of Medicine* **366**, 2474–2482, <https://doi.org/10.1056/NEJMoa1113260> (2012).
- Aneurisk-Team. AneuriskWeb project website, Web Site <http://ecm2.mathcs.emory.edu/aneuriskweb> (2012).
- Juchler, N., Schilling, S., Bijlenga, P., Kurtcuoglu, V. & Hirsch, S. Shape trumps size: image-based morphological analysis reveals that the 3d shape discriminates intracranial aneurysm disease status better than aneurysm size. *Frontiers in Neurology* **13**, 809391, <https://doi.org/10.3389/fneur.2022.809391> (2022).
- Yang, X., Xia, D., Kin, T. & Igarashi, T. Intra: 3d intracranial aneurysm dataset for deep learning. In *Proceedings of the IEEE/CVF Conference on Computer Vision and Pattern Recognition*, 2656–2666, <https://doi.org/10.1109/CVPR42600.2020.00273> (2020).
- Pozo, J. M. & Frangi, A. F. Database of cerebral artery geometries including aneurysms at the middle cerebral artery bifurcation. <https://doi.org/10.15131/shef.data.4806910>
- Vivanco-Suarez, J. *et al.* Dataset on flow diversion procedures performed with the pipeline embolization device, pipeline flex, and surpass streamline for intracranial aneurysms, <https://doi.org/10.1016/j.dib.2022.108299> (2022).
- Di Noto, T. *et al.* Towards automated brain aneurysm detection in TOF-MRA: open data, weak labels, and anatomical knowledge. *Neuroinformatics* **21**, 21–34, <https://openneuro.org/datasets/ds003949> (2023).
- Steinman, D. A. *et al.* Variability of computational fluid dynamics solutions for pressure and flow in a giant aneurysm: the asme 2012 summer bioengineering conference cfd challenge **135**, 021016, <https://doi.org/10.1115/1.4023382> (2013).
- Janiga, G., Berg, P., Sugiyama, S., Kono, K. & Steinman, D. The computational fluid dynamics rupture challenge 2013-phase i: prediction of rupture status in intracranial aneurysms **36**, 530–536 <https://doi.org/10.3174/ajnr.A4157>
- Valen-Sendstad, K. *et al.* Real-world variability in the prediction of intracranial aneurysm wall shear stress: the 2015 international aneurysm cfd challenge. *Cardiovascular engineering and technology* **9**, 544–564, <https://doi.org/10.1007/s13239-018-00374-2> (2018).
- Berg, P. *et al.* Multiple aneurysms anatomy challenge 2018 (match): phase i: segmentation. *Cardiovascular engineering and technology* **9**, 565–581, <https://doi.org/10.1007/s13239-018-00376-0> (2018).
- Berg, P. *et al.* Multiple aneurysms anatomy challenge 2018 (match)-phase ii: rupture risk assessment. *International journal of computer assisted radiology and surgery* **14**, 1795–1804, <https://doi.org/10.1007/s11548-019-01986-2> (2019).

30. Timmins, K. M. *et al.* Comparing methods of detecting and segmenting unruptured intracranial aneurysms on TOF-MRAS: the adam challenge. *Neuroimage* **238**, 118216, <https://doi.org/10.1016/j.neuroimage.2021.118216> (2021).
31. Ivantsits, M. *et al.* Detection and analysis of cerebral aneurysms based on x-ray rotational angiography-the cada 2020 challenge. *Medical image analysis* **77**, 102333, <https://doi.org/10.1016/j.media.2021.102333> (2022).
32. Suarez, J. I. *et al.* Common data elements for unruptured intracranial aneurysms and subarachnoid hemorrhage clinical research: a national institute for neurological disorders and stroke and national library of medicine project. *Neurocritical care* **30**, 4–19 (2019).
33. Wong, G. K. *et al.* Common data elements for unruptured intracranial aneurysm and subarachnoid hemorrhage clinical research: recommendations from the working group on long-term therapies. *Neurocritical care* **30**, 79–86 (2019).
34. Damani, R. *et al.* Common data element for unruptured intracranial aneurysm and subarachnoid hemorrhage: recommendations from assessments and clinical examination workgroup/subcommittee. *Neurocritical care* **30**, 28–35 (2019).
35. de Oliveira Manoel, A. L. *et al.* Common data elements for unruptured intracranial aneurysms and aneurysmal subarachnoid hemorrhage: recommendations from the working group on hospital course and acute therapies—proposal of a multidisciplinary research group. *Neurocritical care* **30**, 36–45 (2019).
36. Bijlenga, P. *et al.* Common data elements for subarachnoid hemorrhage and unruptured intracranial aneurysms: recommendations from the working group on subject characteristics. *Neurocritical care* **30**, 20–27 (2019).
37. Hong, H., Lee, H. & Shin, Y. G. Automatic vessel extraction by patient motion correction and bone removal in brain ct angiography. In *International Congress Series*, vol. 1281, 369–374 (Elsevier, 2005).
38. Moench, T., Neugebauer, M. & Preim, B. Optimization of vascular surface models for computational fluid dynamics and rapid prototyping. In *Second International Workshop on Digital Engineering*, 16–23 (2011).
39. Hellmeier, F. *et al.* Geometric uncertainty in intracranial aneurysm rupture status discrimination: a two-site retrospective study. *BMJ open* **12**, e063051 (2022).
40. Dhar, S. *et al.* Morphology parameters for intracranial aneurysm rupture risk assessment. *Neurosurgery* **63**, 185 (2008).
41. Ujiie, H., Tamano, Y., Sasaki, K. & Hori, T. Is the aspect ratio a reliable index for predicting the rupture of a saccular aneurysm? *Neurosurgery* **48**, 495–503 (2001).
42. Kashiwazaki, D. & Kuroda, S. Size ratio can highly predict rupture risk in intracranial small (<5 mm) aneurysms. *Stroke* **44**, 2169–2173 (2013).
43. Razaghi, R., Biglari, H. & Karimi, A. Risk of rupture of the cerebral aneurysm in relation to traumatic brain injury using a patient-specific fluid-structure interaction model. *Computer Methods and Programs in Biomedicine* **176**, 9–16 (2019).
44. Chen, J., Wang, S., Ding, G., Yang, X. & Li, H. The effect of aneurysmal-wall mechanical properties on patient-specific hemodynamic simulations: two clinical case reports. *Acta Mechanica Sinica* **25**, 677–688 (2009).
45. Güçlü, G. *et al.* Investigation of blood flow behavior in an aneurysm sac using computational fluid dynamics. In *2019 Medical Technologies Congress (TIPTEKNO)*, 1–3 (IEEE, 2019).
46. Sanchez, M. *et al.* Biomechanical assessment of the individual risk of rupture of cerebral aneurysms: a proof of concept. *Annals of biomedical engineering* **41**, 28–40 (2013).
47. Kundu, P. K., Cohen, I. M. & Hu, H. H. *Fluid mechanics* (Academic press, 2015).
48. Torii, R., Oshima, M., Kobayashi, T., Takagi, K. & Tezduyar, T. E. Influence of wall thickness on fluid–structure interaction computations of cerebral aneurysms. *International Journal for Numerical Methods in Biomedical Engineering* **26**, 336–347 (2010).
49. Alwatban, M. R. *et al.* Effects of age and sex on middle cerebral artery blood velocity and flow pulsatility index across the adult lifespan. *Journal of Applied Physiology* **130**, 1675–1683 (2021).
50. Geers, A., Larrabide, I., Morales, H. & Frangi, A. Approximating hemodynamics of cerebral aneurysms with steady flow simulations. *Journal of biomechanics* **47**, 178–185 (2014).
51. Sabernaeemi, A., Barzegar Gerdroodbary, M., Salavatidezfouli, S. & Valipour, P. Influence of stent-induced vessel deformation on hemodynamic feature of bloodstream inside ica aneurysms. *Biomechanics and Modeling in Mechanobiology* 1–15 (2023).
52. Foutarakis, G. N., Yonas, H. & Sclabassi, R. J. Saccular aneurysm formation in curved and bifurcating arteries. *AJNR Am J Neuroradiol* **20**, 1309–1317 (1999).
53. Song, M., Wang, S., Qian, Q., Zhou, Y. & Gong, X. Intracranial aneurysm cta images and 3d models dataset with clinical morphological and hemodynamic data. *Scientific data* <https://doi.org/10.6084/m9.figshare.26965450> (2024).

## Acknowledgements

This research is supported by the Higher Education Scientific Research Project of Anhui Province, Grant No. 2023AH053162, the Clinical Research Incubation Project of the Second Hospital of Anhui Medical University, Grants No. 2021LCZD07, and the National Natural Science Foundation of China, Grants No. 32060193.

## Author contributions

Project Design: M.S., X.G., S.W., Q.Q. Data collection and anonymization: X.G., S.W., Y.L. 3D modeling and Morphological Measurement: S.W., M.S., Y.Z., X.G. Computational Fluid Dynamics Analysis: S.W., M.S., Y.Z., X.G. Creating the figures: M.S., S.W., Q.Q. Writing the manuscript: M.S., S.W., X.G., Y.Z. All authors have read and approved the final manuscript.

## Competing interests

The authors declare no competing interests.

## Additional information

**Supplementary information** The online version contains supplementary material available at <https://doi.org/10.1038/s41597-024-04056-8>.

**Correspondence** and requests for materials should be addressed to X.G.

**Reprints and permissions information** is available at [www.nature.com/reprints](http://www.nature.com/reprints).

**Publisher's note** Springer Nature remains neutral with regard to jurisdictional claims in published maps and institutional affiliations.



**Open Access** This article is licensed under a Creative Commons Attribution-NonCommercial-NoDerivatives 4.0 International License, which permits any non-commercial use, sharing, distribution and reproduction in any medium or format, as long as you give appropriate credit to the original author(s) and the source, provide a link to the Creative Commons licence, and indicate if you modified the licensed material. You do not have permission under this licence to share adapted material derived from this article or parts of it. The images or other third party material in this article are included in the article's Creative Commons licence, unless indicated otherwise in a credit line to the material. If material is not included in the article's Creative Commons licence and your intended use is not permitted by statutory regulation or exceeds the permitted use, you will need to obtain permission directly from the copyright holder. To view a copy of this licence, visit <http://creativecommons.org/licenses/by-nc-nd/4.0/>.

© The Author(s) 2024